Harmonic Analysis and Suppression Method of Output Current Distortion for Medium-Voltage Motor Drives With Modular Multilevel Converter

Fangzhou Zhao, Guochun Xiao, *Member, IEEE*, Tianhua Zhu, *Student Member, IEEE*, Tong Zhao, Xu Zheng, and Zhiqian Wu

***Abstract*—The main technical challenge of the medium-voltage motor drives with modular multilevel converter (MMC) is the serious low-frequency fluctuation on the capacitor voltages, and the existing suppression methods inevitably inject high-frequency circulating currents in MMC. However, the output currents are evidently distorted by the large injected components, while little research has been done to study and solve this problem. This paper analyzes and proves the essential interactions between the output current distortion and the injected components, and the specific dominant output harmonic groups are derived and summarized, revealing the nature of the problem, and it can be taken as a favorable reference for the controller designing. Based on the derivations, this paper proposes a novel suppression method for the greatly improved harmonic characteristics of the output currents during the low-frequency operation. The output harmonics can be accurately measured by the proposed control and effectively suppressed for much lower current total harmonic distortion, benefiting for the superior output control performances with improved efficiency. The simulation results on PSCAD/EMTDC and experimental verifications on a 2.2 kW MMC-based motor drive prototype prove the validity of the presented harmonic analysis and suppression method.**

***Index Terms*—Harmonic analysis and suppression, low-frequency fluctuation, modular multilevel converter (MMC), motor drives.**

I. Introduction

THE modular multilevel converter (MMC) has been proved to be a popular and attractive choice in the medium- and high-power applications [1], [2], especially in the high-voltage direct current transmission system [3]. As a beneficial multilevel topology, MMC has many outstanding advantages such as the

Manuscript received November 4, 2018; revised February 6, 2019 and April 9, 2019; accepted April 22, 2019. Date of publication April 30, 2019; date of current version October 18, 2019. This work was supported by the National Natural Science Foundation of China under Project 51277146. Recommended for publication by Associate Editor N. R. Zargari. *(Corresponding author: Fangzhou Zhao.)*

F. Zhao, G. Xiao, T. Zhu, X. Zheng, and Z. Wu are with the State Key Laboratory of Electrical Insulation and Power Equipment, School of Electrical Engineering, Xi'an Jiaotong University, Xi'an 710049, China (e-mail:

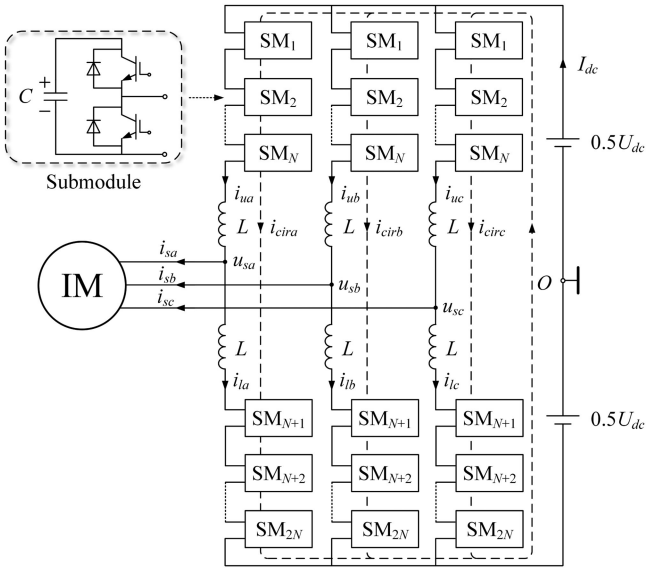

Fig. 1. Basic MMC topology with the motor.

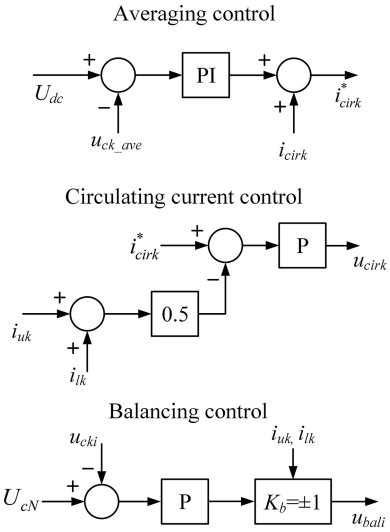

Fig. 2. Traditional MMC control strategy.

driving strategies in various practical applications, the output current distortion should not be neglected, and it is favorable to apply an accommodating control scheme to suppress the harmonics effectively without extra cost and side effects.

This paper derives and proves the inherent relations between the output current distortion and the injected components, and presents a comprehensive analysis of the interactions of the inner and outer characteristics in the MMC-based motor drive. The dominant harmonic groups in the output currents are accurately calculated and summarized in this paper, which provides an accurate and useful reference for the evaluation and controller designing. What is more, this paper proposes an effective method to suppress the harmonic distortion of the output currents caused by the injection on the basis of the derivations above. The proposed control can measure and suppress the harmonics evidently for lower THD of the output current, reducing the loss and benefiting for the superior output control performances and improved efficiency. The validity of the proposed harmonic analysis and suppression method are well proved by the simulations on PSCAD/EMTDC and experimental results on a 2.2 kW MMC-based motor drive prototype.

The outline of this paper is as follows. The analysis of the output current distortion is presented in Section II. The proposed suppression method with low-pass filter (LPF) design is introduced in Section III. The simulation results are given in Section IV. The experiment results are presented in Section V. Finally, the conclusions are drawn in Section VI.

II. Analysis of the Output Current Distortion

Fig. 1 illustrates the topology of the MMC-based motor drive. Clearly, one phase has two arms—upper arm and lower arm, containing totally *N* SMs respectively, and the half-bridge SM topology is common applied as shown in Fig. 1. To suppress the capacitor voltages fluctuation in the start-up and low-speed process, most methods [8]–[15] inject different kinds of circulating current. Theoretically, the injected circulating currents do not flow into the output lines and thus have no direct influences on the output currents. However, the capacitor voltages ripples are significantly affected by the injected components, and they actually associate with the output behaviors of MMC.

In order to derive the relationship between the output current distortion and the injected current, the representative conventional injection method [10] is selected for analysis, and most other improved injection strategies [8], [9], [11]–[15] have similar conclusions. The traditional MMC control strategy [18] including the averaging control, circulating current control, and balancing control is also shown in Fig. 2, where $k = a, b, c$, u_{ck_ave} is the total average capacitor voltage of Phase k, i_{cirk} is the injected circulating current, U_{cN} is the nominal capacitor voltage of one SM, and u_{cki} is the ith SM capacitor voltage, $i = 1, 2, \ldots, 2N$. More information of the widely applied traditional method in Fig. 2 can be found in [10] and [18].

Thus, the injected common-mode voltage u_{com} and circulating current i_{cirk} ($k = a, b, c$) can be described as follows:

$$u_{\mathrm{com}} = -U_{\mathrm{com}} \sin \omega_h t \tag{1}$$

$$i_{\mathrm{cirk}} = \frac{1}{U_{\mathrm{com}}} \left(\frac{2u_{sk}^2}{U_{\mathrm{dc}}} - \frac{U_{\mathrm{dc}}}{2} \right) i_{sk} \sin \omega_h t \tag{2}$$

where U_{com} and ω_h are the amplitude and angular frequency of the injected high-frequency component, which is normally much larger than the fundamental frequency ω, i_{sk} is the output current ($k = a, b, c$ for three-phase), U_{dc} is the dc-link voltage. Taking phase *a* as an example, the output voltage u_{sa} and current i_{sa} are expressed as follows:

$$u_{sa} = \frac{U_{\mathrm{dc}}}{2} m_a = \frac{U_{\mathrm{dc}}}{2} M \sin \omega t \tag{3}$$

$$i_{sa} = I_s \sin(\omega t - \varphi) \tag{4}$$

where m_a is the modulation index, M and I_s are the respective amplitudes, and φ is the phase angle of the output current. Therefore, the upper and lower arm currents are obtained as

follows:

$$i_{uk} = \frac{i_{sk}}{2} + i_{zk} + i_{\rm cirk} \tag{5a}$$

$$i_{lk} = -\frac{i_{sk}}{2} + i_{zk} + i_{\rm cirk} \tag{5b}$$

where i_{zk} is the second-order circulating current that enables the power flow between the phase and the dc-link, and thus it can be expressed as follows [13]:

$$i_{zk} = u_{sk} i_{sk} / U_{\rm dc}. \tag{6}$$

In the low-speed operation of driving the motor, $u_{sk} << U_{\rm dc}$, hence i_{zk} is clearly smaller than i_{sk} and the injected circulating current $i_{\rm cirk}$. The upper and lower arm voltages are defined as follows:

$$u_{uk} = \frac{U_{\rm dc}}{2} - u_{sk} - u_{\rm com} \tag{7a}$$

$$u_{lk} = \frac{U_{\rm dc}}{2} + u_{sk} + u_{\rm com}. \tag{7b}$$

Therefore, the instantaneous power of the upper and lower arm can be expressed as follows:

$$\begin{aligned} p_{uk} = u_{uk} i_{uk} &= \left(\frac{U_{\rm dc}}{2} - u_{sk} - u_{\rm com}\right) \\ &\quad \times \left(\frac{i_{sk}}{2} + i_{zk} + i_{\rm cirk}\right) \\ &= p_{dm1} + p_{dm2} + p_{dm3} + p_{dm4} + p_{dm5} \\ &\quad + p_{cm1} + p_{cm2} + p_{cm3} + p_{cm4} \end{aligned} \tag{8a}$$

$$\begin{aligned} p_{lk} = u_{lk} i_{lk} &= \left(\frac{U_{\rm dc}}{2} + u_{sk} + u_{\rm com}\right) \\ &\quad \times \left(-\frac{i_{sk}}{2} + i_{zk} + i_{\rm cirk}\right) \\ &= -p_{dm1} - p_{dm2} - p_{dm3} - p_{dm4} - p_{dm5} + p_{cm1} \\ &\quad + p_{cm2} + p_{cm3} + p_{cm4} \end{aligned} \tag{8b}$$

where

$$\begin{cases} p_{dm1} = U_{\rm dc} i_{sk}/4 \\ p_{dm2} = -u_{sk} i_{zk} \\ p_{dm3} = -u_{\rm com} i_{\rm cirk} \\ p_{dm4} = -u_{sk} i_{\rm cirk} \\ p_{dm5} = -u_{\rm com} i_{zk} \end{cases} \tag{9a}$$

$$\begin{cases} p_{cm1} = U_{dc} i_{\rm cirk}/2 \\ p_{cm2} = U_{dc} i_{zk}/2 \\ p_{cm3} = -u_{sk} i_{sk}/2 \\ p_{cm4} = -u_{\rm com} i_{sk}/2. \end{cases} \tag{9b}$$

It can be seen that the instantaneous powers of the upper and lower arms in (8) contain the common-mode terms p_{cm1}–p_{cm4} and differential-mode terms p_{dm1}–p_{dm5}. Clearly, the low-frequency fluctuation is mainly caused by p_{dm1} and p_{dm2}, and the low-frequency part of the injected term p_{dm3} is designed to suppress the low-frequency power ripple, which gives $p_{dm1} + p_{dm2} + [p_{dm3}]_{\rm low-frequency} = 0$. Besides, in the low-frequency condition, the output voltage u_{sk} is much less than the dc voltage $U_{\rm dc}$ ($u_{sk} << U_{\rm dc}$), and the injected current $i_{\rm cirk}$ is much larger than the currents i_{zk} ($i_{\rm cirk} \gg i_{zk}$). As a result, the remained dominant terms with the injection in (8) are p_{cm1}, p_{cm4}, p_{dm4} and the high-frequency part of p_{dm3}. Thus, the upper and lower arm powers are simplified as follows:

$$p_{uk} \approx p_{cm1} + p_{cm4} + [p_{dm3}]_{\rm high-frequency} + p_{dm4} \tag{10a}$$

$$p_{lk} \approx p_{cm1} + p_{cm4} - [p_{dm3}]_{\rm high-frequency} - p_{dm4}. \tag{10b}$$

Then, the energy fluctuation of the upper and lower arms should be

$$\tilde{e}_{uk} = \int p_{uk} dt \tag{11a}$$

$$\tilde{e}_{lk} = \int p_{lk} dt. \tag{11b}$$

The energy fluctuation in (11) is buffered by all the capacitors in the arms. Assume the nominal dc capacitor voltage is $U_{\rm dc}/N = U_{cN}$, and $\tilde{u}_{cuk}$ and $\tilde{u}_{clk}$ are the capacitor voltage ripple of upper and lower arms, thus the energy of the arm can be written as follows:

$$\begin{aligned} E_{cr} = E_{cr0} + \tilde{e}_{rk} &= \frac{1}{2} NC (U_{cN} + \tilde{u}_{crk})^2 \\ &= \frac{1}{2} NC U_{cN}^2 + NC U_{cN} \tilde{u}_{crk} + \frac{1}{2} NC \tilde{u}_{crk}^2 \end{aligned} \tag{12}$$

where $r = u$ and l for upper and lower arms, E_{cr0} is the dc component of the energy stored in the r arms, $\tilde{e}_{rk}$ is the energy ripple of the r arm, $\tilde{u}_{crk}$ is the capacitor voltage ripple of the r arm, and C is the SM capacitance. Obviously, the voltage ripple $\tilde{u}_{crk}$ is much smaller than U_{cN}, and hence the capacitor energy ripple is mainly determined by $NCU_{cN}\,\tilde{u}_{crk}$. Therefore, the energy ripple can be simplified as follows:

$$\tilde{e}_{rk} \approx NC U_{cN} \tilde{u}_{crk}. \tag{13}$$

Then the capacitor voltage ripple $\tilde{u}_{crk}$ can be derived as follows:

$$\tilde{u}_{crk} = \frac{\tilde{e}_{rk}}{NC U_{cN}}. \tag{14}$$

As a result, considering the capacitor voltage ripples and the switching harmonics of the phase-shifted carrier-pulsewidth modulation, the actual output voltage is derived in (15) shown at bottom of the next page, as follows, and (16) gives the detailed

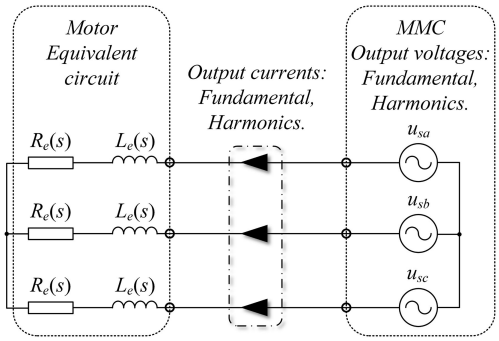

Fig. 3. Equivalent circuit of the induction motor with MMC output voltages in steady-state.

expressions of the terms $u_{\rm fun}$, u_{h1}, u_{h2}, u_{h3}, u_{h4} in (15)

$$\begin{cases} u_{\rm fun} = \dfrac{1}{2} m_k U_{\rm dc} \\ u_{h1} = u_{\rm com} \\ u_{h2} = \dfrac{1}{4} N \left(\tilde{u}_{clk} - \tilde{u}_{cuk} \right) \\ u_{h3} = \dfrac{1}{4} m_k N \left(\tilde{u}_{clk} + \tilde{u}_{cuk} \right) \\ u_{h4} = \dfrac{u_{\rm com}}{2U_{\rm dc}} N \left(\tilde{u}_{clk} + \tilde{u}_{cuk} \right). \end{cases} \tag{16}$$

Clearly, the harmonic components of the switching frequency in (15) are $N\omega_s$ and higher, and they are far away from the injected components ω_h and the fundamental component ω. As a result, this paper mainly focuses on studying the harmonics caused by the injected components, while the switching frequency components have small influences on the studied harmonics near ω_h, and it is also too complicated to calculate with detailed components $O(N\omega_s)$ and higher terms.

Consequently, neglecting the harmonics of the switching frequency, the output voltage in (15) still contains complicated harmonic components caused by the injection, and the motor can be treated as a passive load in steady-state for a specific slip ratio *s*. The harmonics in the output voltages definitely lead to the harmonic currents through the equivalent inductor and resistor of the induction motor [19], [20], shown in Fig. 3, which reveals the nature of the output current distortion problem. As a result, the output harmonic voltages are the direct cause that lead to the output current distortion. The existing harmonics brought by the injection can be divided into the dominant components and the higher order harmonics in the following analysis.

A. Dominant Harmonic Components

Taking phase *a* ($k = a$) as an example, u_{sa} is divided into several terms that contains different harmonics shown in (15) and (16).

1) $u_{\rm fun}$: $u_{\rm fun}$ is the fundamental output voltage that drives the motor and generates the fundamental currents. It is obtained from the motor control loops such as the *Voltage/frequency* (*V/f*) control [19], [20], field-oriented control (FOC) [21] or the vector control [22], direct torque control (DTC) [23], [24], and so on.
2) u_{h1}: u_{h1} is the injected common-mode voltage $u_{\rm com}$ for suppressing the low-frequency ripple. $u_{\rm com}$ is the same in three phases, thus no zero-sequence harmonic current exists in the three-phase three-wire topology shown in Fig. 3.
3) u_{h2}: u_{h2} is caused by the difference of the upper and lower arm voltage ripples. Apparently, the modulation index *M* is relatively small in the low-frequency condition. Therefore, inserting (1)–(4), (6), (8), (11), (14) into (16), and neglecting the smaller terms and zero-sequence parts, the dominant components of u_{h2} is derived as follows:

$$\begin{aligned} u_{h2} \approx & \frac{U_{h2I}}{2\omega_h + \omega} \cos\left[(2\omega_h + \omega) t - \varphi \right] \\ & - \frac{U_{h2I}}{2\omega_h - \omega} \cos\left[(2\omega_h - \omega) t + \varphi \right] \\ & - \frac{U_{h2II}}{\omega_h + 2\omega} \cos\left[(\omega_h + 2\omega) t - \varphi \right] \\ & - \frac{U_{h2II}}{\omega_h - 2\omega} \cos\left[(\omega_h - 2\omega) t + \varphi \right] \end{aligned} \tag{17}$$

where

$$\begin{cases} U_{h2I} = \dfrac{NI_s}{16C} \\ U_{h2II} = \dfrac{MNI_s U_{\rm dc}}{32CU_{\rm com}}. \end{cases} \tag{18}$$

$$\begin{aligned} u_{sk} &= \frac{1}{2}\left(u_{lk} - u_{uk}\right) = \frac{1}{2}\left[\left(\frac{U_{\rm dc}}{2} + u_{sk} + u_{\rm com}\right) - \left(\frac{U_{\rm dc}}{2} - u_{sk} - u_{\rm com}\right)\right]_{\rm PSC-PWM} \\ &= \frac{1}{2}\left\{ N\frac{U_{\rm dc}/2 + u_{sk} + u_{\rm com}}{U_{\rm dc}}\left(U_{cN} + \tilde{u}_{clk}\right) - N\frac{U_{\rm dc}/2 - u_{sk} - u_{\rm com}}{U_{\rm dc}}\left(U_{cN} + \tilde{u}_{cuk}\right) + O\left(N\omega_s\right) \right. \\ &\quad \left. + O\left(2N\omega_s\right) + \cdots \right\}_{\rm PSC-PWM} \\ &\approx \frac{1}{2}\left[\left(1 + m_k + \frac{2u_{\rm com}}{U_{\rm dc}}\right)\frac{N\left(U_{cN} + \tilde{u}_{clk}\right)}{2} - \left(1 - m_k - \frac{2u_{\rm com}}{U_{\rm dc}}\right)\frac{N\left(U_{cN} + \tilde{u}_{cuk}\right)}{2}\right] \\ &= u_{\rm fun} + u_{h1} + u_{h2} + u_{h3} + u_{h4} \end{aligned} \tag{15}$$

TABLE I
DOMINANT HARMONICS IN u_{h2}, u_{h3}, AND u_{h4}

Symbol	Dominant harmonics
u_{h2}	ω_h-2ω, ω_h+2ω, 2ω_h+ω, 2ω_h-ω
u_{h3}	ω_h-2ω, ω_h+2ω
u_{h4}	2ω_h+ω, 2ω_h-ω

Consequently, the harmonic components in u_{h2} are around ω_h and $2\omega_h$, and the detailed frequencies of the dominant terms that bring the output harmonic currents are $\omega_h + 2\omega$, ω_h–2ω, $2\omega_h + \omega$, and $2\omega_h$–ω.

4) u_{h3}: u_{h3} is caused by the sum of the upper and lower arm voltage ripples. Similarly, to focus on the dominant harmonics, the small terms in u_{h3} are neglected to simplify the calculation, such as the terms that multiplied by M^3. Thus, u_{h3} can be organized as follows:

$$u_{h3} \approx -\frac{U_{h3I}}{\omega_h + \omega}\cos\left[(\omega_h + 2\omega)\,t - \varphi\right] - \frac{U_{h3I}}{\omega_h - \omega}\cos\left[(\omega_h - 2\omega)\,t + \varphi\right] \tag{19}$$

where

$$U_{h3I} = \frac{MNI_s}{32C}\left(\frac{U_{\rm dc}}{U_{\rm com}} - \frac{2U_{\rm com}}{U_{\rm dc}}\right). \tag{20}$$

Therefore, the dominant harmonics in u_{h3} are around ω_h, and the detailed frequencies are ω_h–2ω and $\omega_h + 2\omega$.

5) u_{h4}: u_{h4} is also caused by the sum of the upper and lower arm voltage ripples. Focusing on the dominant harmonics, and substituting (1)–(4), (6), (8), (11), (14) into (16), u_{h4} is obtained

$$u_{h4} \approx -\frac{U_{h4I}}{\omega_h + \omega}\cos\left[(2\omega_h + \omega)\,t - \varphi\right] + \frac{U_{h4I}}{\omega_h - \omega}\cos\left[(2\omega_h - \omega)\,t + \varphi\right] \tag{21}$$

where

$$U_{h4I} = \frac{NU_{\rm com}I_s}{16CU_{\rm dc}}\left(\frac{U_{\rm dc}}{U_{\rm com}} - \frac{2U_{\rm com}}{U_{\rm dc}}\right). \tag{22}$$

Equation (21) indicates that the dominant harmonics in u_{h4} are around $2\omega_h$, and the frequencies are $2\omega_h + \omega$, $2\omega_h$–ω.

Above all, the output harmonic voltages are caused by u_{h2}, u_{h3}, and u_{h4}. In summary, Table I lists the frequencies of the dominant harmonics in u_{h2}, u_{h3}, and u_{h4}.

Hence, considering that ω_h is much larger than ω for simplification, the total dominant harmonics around ω_h in u_{h2} and u_{h3} are calculated as follows:

$$u_{\omega_h+2\omega} = \left(-\frac{U_{h2II}}{\omega_h + 2\omega} - \frac{U_{h3I}}{\omega_h + \omega}\right)\cos\left[(\omega_h + 2\omega)\,t - \varphi\right] \approx -\frac{NMI_s}{32\omega_h C}\left(\frac{3U_{\rm dc}}{2U_{\rm com}} - \frac{2U_{\rm com}}{U_{\rm dc}}\right)\cos[(\omega_h + 2\omega)\,t - \varphi]. \tag{23a}$$

$$u_{\omega_h-2\omega} = \left(-\frac{U_{h2II}}{\omega_h - 2\omega} - \frac{U_{h3I}}{\omega_h - \omega}\right)\cos\left[(\omega_h - 2\omega)\,t + \varphi\right] \approx -\frac{NMI_s}{32\omega_h C}\left(\frac{3U_{\rm dc}}{2U_{\rm com}} - \frac{2U_{\rm com}}{U_{\rm dc}}\right)\cos[(\omega_h - 2\omega)\,t + \varphi]. \tag{23b}$$

And the total dominant harmonics around $2\omega_h$ in u_{h2} and u_{h4} are calculated as follows:

$$u_{2\omega_h+\omega} = \left(\frac{U_{h2I}}{2\omega_h + \omega} - \frac{U_{h4I}}{\omega_h + \omega}\right)\cos\left[(2\omega_h + \omega)\,t - \varphi\right] \approx -\frac{NI_s}{32\omega_h C}\left(1 - \frac{4U_{\rm com}^2}{U_{\rm dc}^2}\right)\cos\left[(2\omega_h + \omega)\,t - \varphi\right] \tag{24a}$$

$$u_{2\omega_h-\omega} = \left(-\frac{U_{h2I}}{2\omega_h - \omega} + \frac{U_{h4I}}{\omega_h - \omega}\right)\cos\left[(2\omega_h - \omega)\,t + \varphi\right] \approx \frac{NI_s}{32\omega_h C}\left(1 - \frac{4U_{\rm com}^2}{U_{\rm dc}^2}\right)\cos\left[(2\omega_h - \omega)\,t + \varphi\right]. \tag{24b}$$

Equation (23) indicates that the amplitudes of $u_{\omega h+2\omega}$ and $u_{\omega h-2\omega}$ are multiplied by the modulation M, while $u_{2\omega h+\omega}$ and $u_{2\omega h-\omega}$ in (24) are not associated with M. Thus, the proportion of ω_h–2ω and $\omega_h + 2\omega$ harmonics become larger when the speed or the load torque increases, since M grows.

Besides, the magnitude of $u_{\omega h-2\omega}$ is actually slightly larger than $u_{\omega h+2\omega}$, and $u_{2\omega h-\omega}$ is also larger than $u_{2\omega h+\omega}$, which can be easily obtained from (17), (19), and (21). While as mentioned above, ω_h is much larger than ω, thus ω_h–$\omega \approx 2\omega_h + \omega \approx \omega_h$, and $2\omega_h$–$\omega \approx 2\omega_h + \omega \approx 2\omega_h$. Therefore, the differences can be accepted and the amplitudes are the same in (23a) and (23b) and (24a) and (24b) with simplification. Obviously, the difference of the magnitudes gradually increases with the fundamental frequency ω, but it is very small in low-speed regions and consequently it can be accepted.

As a result, the injection evidently causes the output voltage harmonics through the capacitor voltage ripples, and the output currents of the motor are thus distorted. The analysis and derivations above prove the dominant harmonic voltages are around ω_h (ω_h–2ω and $\omega_h + 2\omega$) and $2\omega_h$ ($2\omega_h + \omega$ and $2\omega_h$–ω), and they accordingly lead to the output harmonic currents of the same frequencies.

B. Higher Order Harmonic Components

The output harmonic currents also appear in the arm currents of the MMC as shown in (5), and the distorted arm currents further generate more output harmonic voltages of higher frequencies and thus lead to more higher order output harmonic currents. To be detailed, the output harmonics around $2\omega_h$ will lead to the harmonics around $4\omega_h$ with reduced amplitude, and the $4\omega_h$ harmonics will also bring $6\omega_h$ harmonics with further decreased amplitude, and so on. Similarly, the output harmonic currents around ω_h calculated above will result in the subsequent $3\omega_h$ and $5\omega_h$ harmonics, and so on. However, the amplitudes

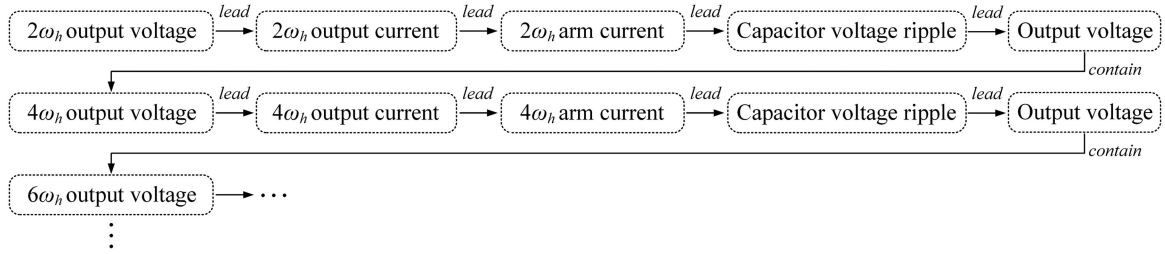

Fig. 4. Relations of the generated higher order harmonics of $2\omega_h$, $4\omega_h$, $6\omega_h$.

of higher order harmonics decrease evidently, and consequently the minor high-frequency components can be neglected.

To prove it, taking the output harmonics around $2\omega_h$ ($2\omega_h + \omega$ and $2\omega_h$–ω) as examples, they are regarded as the known quantities to verify that they further lead to the output harmonic currents of $4\omega_h + \omega$ and $4\omega_h$–ω with reduced amplitudes. Hence, the corresponding output harmonic current around $2\omega_h$ of phase a i_{a2} is expressed as follows:

$$i_{a2} = I_{2I}\sin[(2\omega_h - \omega)t - \varphi_{2I}] + I_{2II}\sin[(2\omega_h + \omega)t - \varphi_{2II}] \tag{25}$$

where I_{2I}, I_{2II} and φ_{2I}, φ_{2II} are the amplitudes and phases of the $2\omega_h$–ω and $2\omega_h + \omega$ harmonic currents. Clearly, the harmonic currents in (25) are much smaller than the fundamental current.

Therefore, the upper and lower arm currents should be rewritten as follows:

$$i_{ua} = \frac{i_{sa} + i_{a2}}{2} + i_{za} + i_{\text{cira}} \tag{26a}$$

$$i_{la} = -\frac{i_{sa} + i_{a2}}{2} + i_{za} + i_{\text{cira}}. \tag{26b}$$

As the added output harmonic current, i_{a2} can be directly inserted into i_{sa} in (1)–(16) to calculate the additional harmonic voltages caused by i_{a2}. Hence, substituting i_{a2} into i_{sa}, the harmonic voltages around $4\omega_h$ in u_{h2} and u_{h4} led by i_{a2} are obtained as follows:

$$\begin{aligned} u_{h2a2}(4\omega_h t) \approx\ & \frac{NI_{2I}}{16C(4\omega_h - \omega)}\cos[(4\omega_h - \omega)t - \varphi_{2I}] \\ & + \frac{NI_{2II}}{16C(4\omega_h + \omega)}\cos[(4\omega_h + \omega)t - \varphi_{2II}] \end{aligned} \tag{27a}$$

$$\begin{aligned} u_{h4a2}(4\omega_h t) \approx\ & -\frac{NU_{\text{com}}I_{2I}}{16CU_{\text{dc}}(3\omega_h - \omega)}\left(\frac{U_{\text{dc}}}{U_{\text{com}}} - \frac{2U_{\text{com}}}{U_{\text{dc}}}\right) \\ & \times \cos[(4\omega_h - \omega)t - \varphi_{2I}] \\ & - \frac{NU_{\text{com}}I_{2II}}{16CU_{\text{dc}}(3\omega_h + \omega)}\left(\frac{U_{\text{dc}}}{U_{\text{com}}} - \frac{2U_{\text{com}}}{U_{\text{dc}}}\right) \\ & \times \cos[(4\omega_h + \omega)t - \varphi_{2II}]. \end{aligned} \tag{27b}$$

Both u_{h2a2} and u_{h4a2} contain the harmonics around $4\omega_h$ ($4\omega_h + \omega$ and $4\omega_h$–ω), which generate the corresponding $4\omega_h + \omega$ and $4\omega_h$–ω output harmonic currents. The amplitudes of these harmonics around $4\omega_h$ in u_{h2a2} and u_{h4a2} are much less than the dominant harmonics (ω_h–2ω, $\omega_h + 2\omega$, $2\omega_h + \omega$, and $2\omega_h$–ω), but they do exist in the output currents.

What is more, this relation can be extended. The harmonic currents around $4\omega_h$ (i_{a4}) can also generate the harmonic currents around $6\omega_h$ with reduced amplitudes, which can be proved by similar derivations as (25)–(27). The reason for this relationship lies in the calculation of u_{h2} and u_{h4}—the output harmonic currents are multiplied by $\cos(2\omega_h t)$ or multiplied by $\cos(\omega_h t)$ twice, thus the phases of the generated output harmonics are added by $2\omega_h t$. Similarly, the dominant harmonics around ω_h in u_{h3} have the same characteristics, and the harmonics around $3\omega_h$ and $5\omega_h$ can also be found and derived as (25)–(27). However, the amplitudes of higher order harmonics decrease evidently, hence it is unnecessary to consider the harmonic currents higher than $6\omega_h$. The relations of the generated higher order harmonics of $2\omega_h$, $4\omega_h$, $6\omega_h$ described above are depicted in Fig. 4.

In summary, the harmonics in the output currents can be finally divided into two groups.

1) Around ω_h, $3\omega_h$, $5\omega_h$, etc. The dominant harmonics are ω_h–2ω and $\omega_h + 2\omega$ in this group. With the increase of the frequency, the amplitudes of higher order harmonics decrease evidently.
2) Around $2\omega_h$, $4\omega_h$, $6\omega_h$, etc. The dominant harmonics are $2\omega_h + \omega$ and $2\omega_h$–ω in this group. With the increase of the frequency, the amplitudes of higher order harmonics decrease evidently.

In conclusion, the essential reason for the output current distortion is the output harmonic voltage caused by the capacitor voltage ripples and the injected components. The dominant harmonic currents of two groups summarized above are around ω_h (ω_h–2ω, $\omega_h + 2\omega$) and $2\omega_h$ ($2\omega_h + \omega$, $2\omega_h$–ω).

III. Proposed Suppression Method With LPF Design

A. Proposed Suppression Method

The block diagram of the proposed suppression method is illustrated in Fig. 5. The complete strategy for the MMC-based motor drive includes the motor control, MMC control, and the proposed suppression control as shown in Fig. 5. Different motor controls can be applied, such as the *V/f* control [19], [20], FOC [21], [22], DTC [23], [24], and the conventional MMC strategy including the averaging, balancing, and circulating current control is given in [10], and other advanced MMC strategies can also be used. The added proposed control measures the output harmonic currents and suppresses them by the feedback and feedforward control.

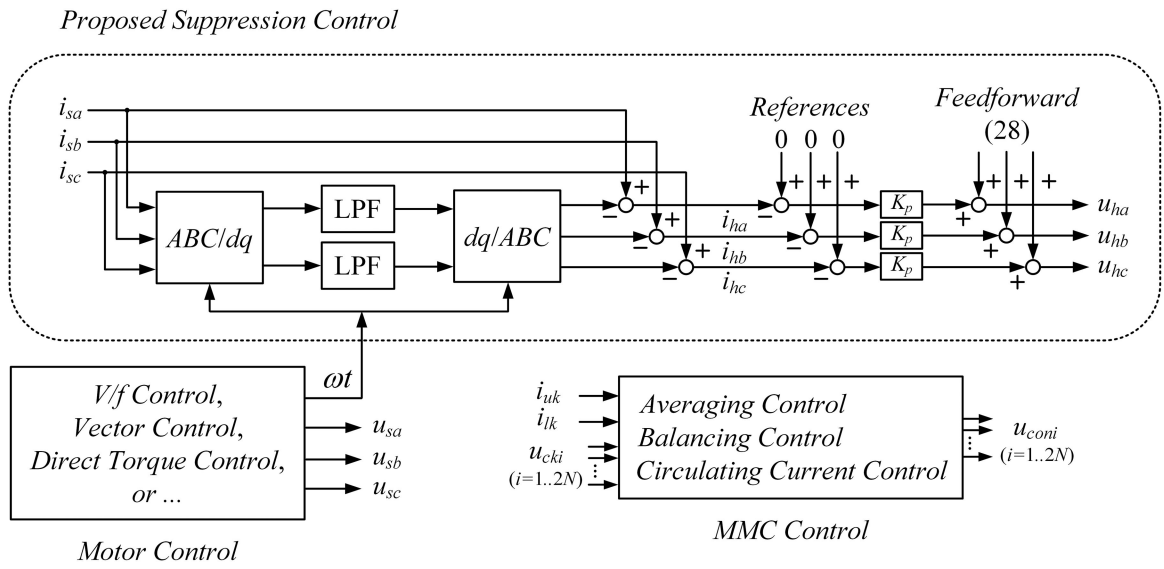

Fig. 5. Block diagram of the proposed suppression control.

It should be clarified that the fundamental output distortion is effectively controlled and refrained by the closed-loop motor control in the low-, medium, and high-speed regions, but the motor control shows unsatisfying limitations of the injected high-frequency harmonics in the low-speed region. The proposed suppression control aims to effectively reduce the high-frequency harmonic distortion caused by the injection in the low-speed region. Although the fundamental and harmonic distortion both essentially result from the capacitor voltage ripples, the frequencies of the components are so different, and thus they can be respectively suppressed by different control schemes for superior output performances. The outputs of all the loops above are added together and then distributed to the SMs.

As analyzed above, the output harmonic currents are actually caused by the output harmonic voltages. Therefore, the output current distortion can be suppressed by compensating the output harmonic voltages. The detailed expressions of the existing dominant harmonic voltages around ω_h (ω_h–2ω, $\omega_h + 2\omega$) and $2\omega_h$ ($2\omega_h + \omega$, $2\omega_h$–ω) are derived in (23) and (24), thus the feedforward control can be used to inject the opposite output voltages for suppressing the harmonics. Therefore, combining (23) and (24), the injected output voltages for compensation are expressed as follows:

$$u_{fc} = U_{\omega I}\cos\left[(\omega_h + 2\omega)\,t - \varphi\right] + U_{\omega I}\cos\left[(\omega_h - 2\omega)\,t + \varphi\right] + U_{2\omega}\cos[(2\omega_h + \omega)t - \varphi] - U_{2\omega}\cos[(2\omega_h - \omega)t + \varphi] \tag{28}$$

where

$$\begin{cases} U_{\omega I} = \dfrac{NI_s}{32\omega_h C}\left(\dfrac{3MU_{\rm dc}}{2U_{\rm com}} - \dfrac{2MU_{\rm com}}{U_{\rm dc}}\right) \\ U_{2\omega} = \dfrac{NI_s}{32\omega_h C}\left(1 - \dfrac{4U_{\rm com}^2}{U_{\rm dc}^2}\right). \end{cases} \tag{29}$$

What is more, to reduce the higher order harmonics and improve the control performances, the feedback control loop for the output harmonic currents is applied illustrated in Fig. 5. First, the proposed control measures the output harmonic currents by the coordinate transformation with LPF. Considering that $\omega_h \gg \omega$, the three-phase output currents are transformed into the *dq* rotating coordinate under the fundamental frequency ω through *ABC*-to-*dq* transformation [25], and the dominant fundamental components become the dc term, while the harmonics that should be suppressed are still ac terms. Hence, the LPF is employed to keep the dc term and eliminate the harmonics of ac terms. Then, by applying the *dq*-to-*ABC* inverse transformation [25], the fundamental components without harmonics can be restored. Finally, subtracting the fundamental currents from the original three-phase output currents, the output harmonic currents are accurately obtained. Clearly, the basic principles of the harmonic detection of the proposed method are similar to the active power filter [26], and more information of the harmonic detections can be found in [27]–[29]. The different point in the proposed control is that the angular frequency ωt required in the coordinate transformation can be directly acquired from the motor control as shown in Fig. 5. Hence, it indicates the convenience and practicability of the proposed suppression method since the additional phase-locked loop is not required.

As a result, the harmonics in the output currents are separated, and then the feedback control loop with proportional controller is employed to suppress the harmonics. The references for the three-phase harmonics are zero in Fig. 5, and the proportional controllers (K_p) are used to track the harmonic currents for effectiveness, reliability, and usability. Considering the harmonic components are complicate ac terms with time-varying amplitude and frequency, advanced controllers such as proportional-integral (PI) and proportion-resonant controllers are hard to design with undesirable results, and thus proportional controller is more suitable for this situation in terms of the satisfying dynamic performances, stability, and simplicity.

The output voltages of the proportional controller are added with the compensated voltages (28) in feedforward loop to improve the dynamic control performances. Finally, the obtained control voltages u_{hk} $(k = a, b, c)$ of the proposed suppression

are superposed to the other control voltages of the system, including the motor control (*V/f* or other strategies for the motor) and MMC control (averaging, balancing and circulating current control) in Fig. 5. It should be mentioned the other advanced strategies could also be used since the proposed suppression method is independent of the MMC control, such as the capacitor voltages balancing, and it has little undesirable influence on the inner characteristics of MMC. Therefore, the final control voltage references for each SM ($i = 1 \ \ldots \ N$ for upper arm, $i = N+1 \ \ldots \ 2N$ for lower arm) are obtained as follows:

$$u^*_{cki} = u_{\text{coni}} - \frac{u_{sk} + u_{hk} + u_{\text{com}}}{N} + \frac{U_{\text{dc}}}{2N} \ \ (i = N+1 \ldots 2N) \tag{30a}$$

$$u^*_{cki} = u_{\text{coni}} + \frac{u_{sk} + u_{hk} + u_{\text{com}}}{N} + \frac{U_{\text{dc}}}{2N} \times (i = N+1 \ldots 2N) \tag{30b}$$

where u_{hk} $(k = a, \ b, \ c)$ are the control voltages of the proposed suppression method, u_{sk} are the output control voltages for the motor, u_{coni} are the sums of the averaging, balancing, circulating current control voltages for MMC, and u_{com} is the injected common-mode voltage. In addition, other injection methods [8]–[15] can also be employed with the proposed control, since the proposed method aims to reduce the harmonic distortion of the output currents and has little influence on the injection methods. Thus, different waveforms and combinations of the injected components can be applied, and the proposed method is able to measure and suppress the output harmonic currents caused by the injections evidently and efficiently.

B. LPF Design

The proposed suppression control highly relies on the LPF-based harmonics detection, which directly affects the accuracy of control references. Hence, it is significant to design the cut-off frequency of the LPF properly in consideration of the variation of the motor speed.

First of all, it should be clarified that the cut-off frequency and the detailed LPF is not changing online with the motor speed in the proposed control strategy. The system injects large components in the low-speed region to suppress the fluctuation, while the components are evidently reduced in the medium- and high-speed regions. Hence, the LPF mainly operates in the low-speed region, and the difference between the fundamental output frequency ω and the high frequency of the injected component ω_h is quite large $(\omega_h \gg \omega)$ [8]–[15]. As a result, it is feasible to apply the LPF with the fixed cut-off frequency when the motor speed varies in the low-speed region.

To be detailed, the range of the low-frequency region f_o $(\omega = 2\pi f_o)$ is about 0–15 Hz, and the frequency of the injected component f_h $(\omega_h = 2\pi f_h)$ should be less than 1/10 of the switching frequency f_s [10], [13], and at least four times higher than the output fundamental frequency f_o (i.e., $4f_o \leq f_h \leq f_s/10$) [11]. According to the proposed suppression control in Fig. 5, by applying the *ABC/dq* coordinate transformation, the fundamental output current becomes the dc terms. As for the output harmonic currents, although the frequencies change after the transformation, they are still transformed into ac terms at around ω_h, $2\omega_h$, etc., because the injected frequency ω_h is much larger than the fundamental frequency ω in the low-speed region [8]–[15]. Consequently, considering the high-frequency harmonics and the dynamic control performances of the fundamental components, it is recommended that the cut-off frequency f_c of the LPF is designed to be less than 1/10 of the injected frequency f_h and higher than 1/6 of the fundamental frequency f_o (i.e., $f_o/6 \leq f_c \leq f_h/10$) in the practical engineering. The frequencies of the injected components f_h in the experimental results are 50 and 62.5 Hz to verify the proposed derivations, and f_c is set to be 2.5 Hz, which is obviously low enough to separate the output harmonics. The traditional digital second-order LPF is adopted in this paper for simplicity and effectiveness, and other types of LPF could also be applied. The transfer function of the traditional second-order LPF is

$$G(s) = \frac{\omega_c^2}{s^2 + 2\xi\omega_c s + \omega_c^2} \tag{31}$$

where ω_c is the cut-off angular frequency, ξ is the damping ratio. Therefore, when f_c is designed to be 2.5 Hz $(\omega_c = 2\pi f_c = 5\pi)$, and ξ is 0.71 for –3 dB on f_c, Fig. 6 shows the bode diagram of the traditional second-order LPF. The magnitude of 50 Hz is –52 dB, indicating that the output harmonics can be effectively suppressed by the LPF.

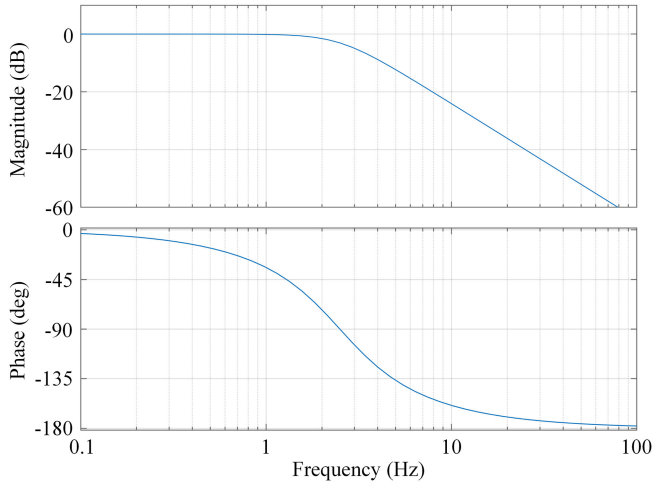

Fig. 6. Bode diagram of the traditional second-order filter.

TABLE II
PARAMETERS OF THE SIMULATIONS

Parameters of MMC			
Quantity	Value	Quantity	Value
Rated power	1.5 MVA	Nominal capacitor voltage	1 kV
Rated DC voltage	18 kV	SM capacitance	2.2 mF
Rated frequency	50 Hz	Arm inductance	4 mH
Number of SMs per arm	18	Carrier frequency	500 Hz
Parameters of induction motor			
Rated power	1.25 MW	Rated speed	1485 r/min
Rated voltage (L-L)	10 kV	Rated torque	8039 Nm
Rated frequency	50 Hz	Pole-pair number	2

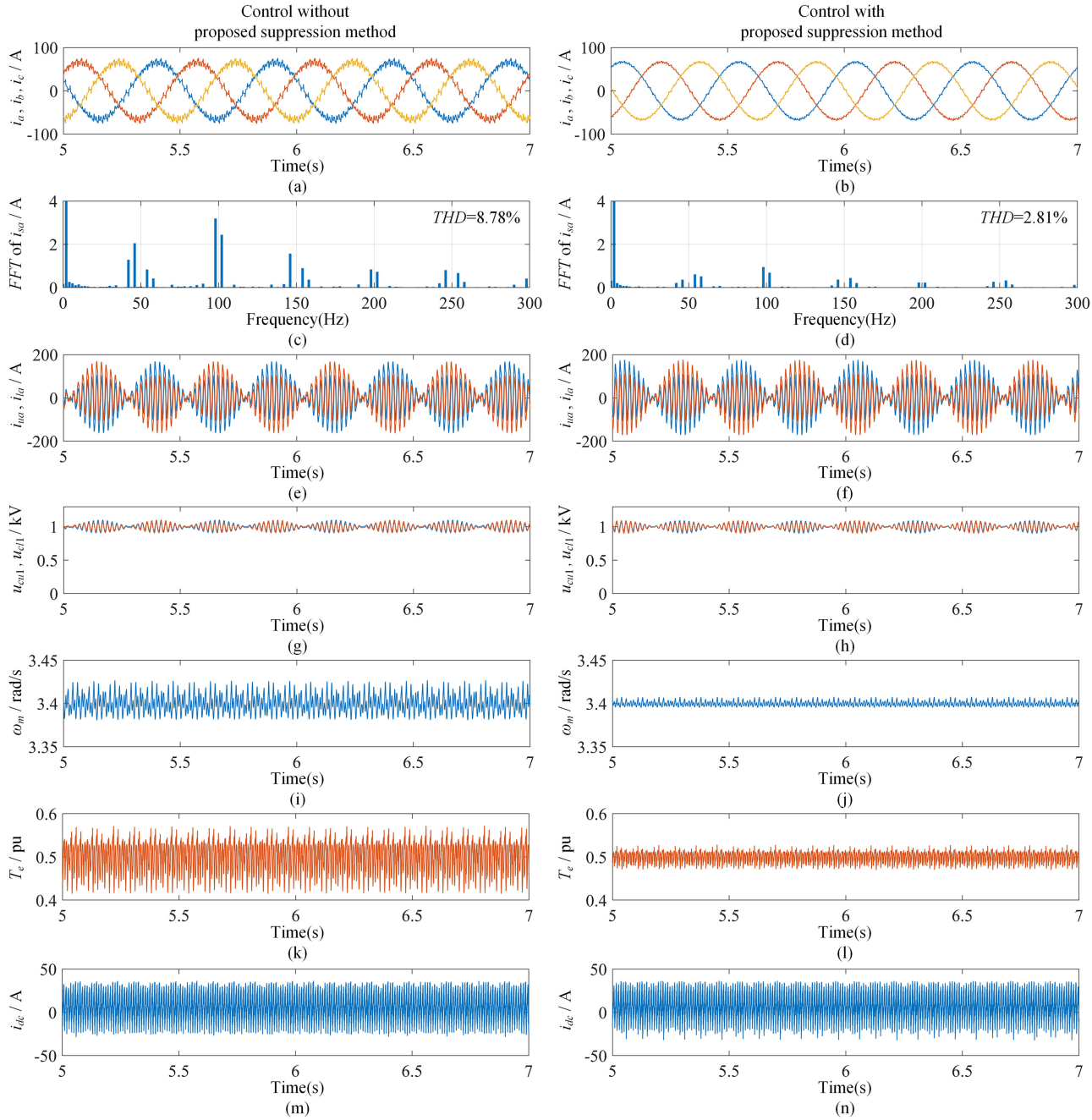

Fig. 7. Comparisons results of the control without and with the proposed suppression at 2 Hz output frequency.

In conclusion, based on the analysis and derivations of the output harmonic currents above, the proposed control effectively reduces the distortion of the output currents by compensating the harmonic voltages through the feedforward and feedback control loop. The harmonics in the output currents can be clearly measured and suppressed by the proposed method for much lower THD and satisfying output control performances with improved efficiency of the motor.

IV. Simulation Results

Simulations of a 1.25 MW/10 kV induction motor drive with MMC are conducted on PSCAD/EMTDC to verify the proposed suppression control. The parameters of the MMC and motor in simulations are listed in Table II. The traditional injection method [10] is applied to suppress the low-frequency fluctuations. The speed of the motor is controlled at 32.2 r/min and the actual frequency of the output current is very close to 2 Hz when the motor is under 50% rated load torque. In this way, it is easier and clearer to observe and analyze the harmonics with the fundamental currents in simulations as the frequency is an integer, and the load torque is also quite large.

The fundamental frequency is very low, which is only 0.04 p.u. of the nominal frequency, and the frequency of the injected components is 50 Hz. Therefore, according to the analysis in Section II, the dominant harmonics are ω_h–2ω, $\omega_h + 2\omega$,

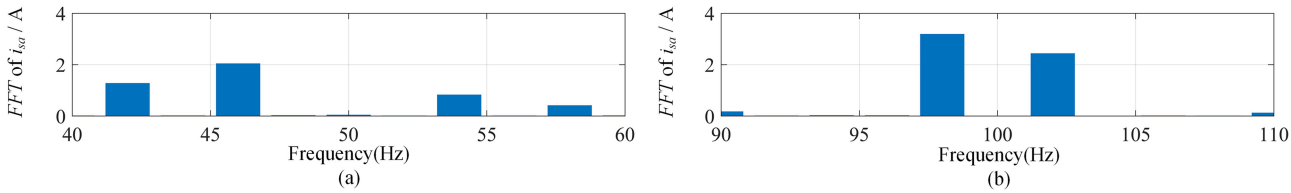

Fig. 8. Expanded FFT of the harmonics around 50 and 100 Hz in Fig. 7(c).

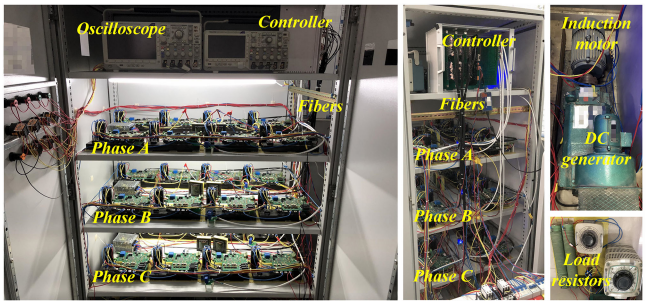

Fig. 9. Photograph of the experimental motor drive with MMC.

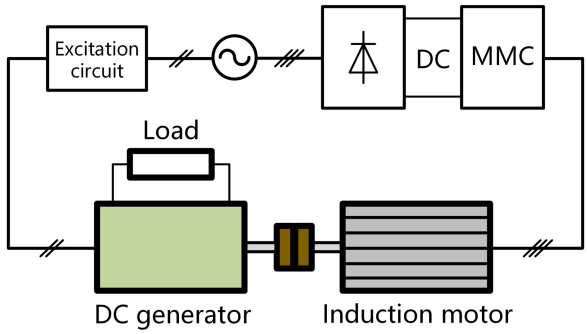

Fig. 10. Overview of the MMC setup.

TABLE III
PARAMETERS OF THE EXPERIMENTAL PROTOTYPE

Parameters of MMC	
Quantity	Value
Rated power	2.5 kVA
Rated DC voltage	400 V
Fundamental frequency	50 Hz
Number of SMs per arm	4
Nominal SM capacitor voltage	100 V
SM capacitance	2 mF
Arm inductance	1.5 mH
Switching frequency	2 kHz
Parameters of induction motor	
Quantity	Value
Rated power	2.2 kW
Rated voltage (L-L RMS)	380 V
Rated frequency	50 Hz
Rated speed	1430 r/min
Rated torque	14.7 Nm
Pole-pair number	2

$2\omega_h + \omega$, and $2\omega_h - \omega$, and they are calculated as 46, 54, 98, and 102 Hz. Hence, to prove the effectiveness of the proposed analysis and method, the comparisons results of the control without and with the proposed suppression at 2 Hz output frequency under half rated load torque are presented in Fig. 7. The influences of the MMC controls in the comparative simulation and experiment results are excluded. The MMC controls are properly designed, adjusted, and applied, and the only difference between the two groups in the comparative results is with or without the proposed suppression control. All the other control loops including the designed control parameters of the comparative sets are identical to focus on the verifications of the proposed suppression control. Besides, the output voltages of the MMC controls only have very small influences on the output harmonic distortion, since they are much smaller than the dominant components. As a result, the output voltages of the MMC controls are commonly neglected to focus on the fluctuation and harmonic analysis of the major parts [8]–[15].

The three-phase output currents are shown in Fig. 7(a) and (b). Apparently, the output currents of the control without the proposed method are evidently distorted by the injection as shown in Fig. 7(a). While with the proposed suppression control, the harmonics in the output currents are greatly reduced in Fig. 7(b), demonstrating the effectiveness of the proposed method. Fig. 7(c) and (d) give the results of the fast Fourier transform (FFT) analysis of the output currents (phase *a*, blue lines), respectively, in Fig. 7(a) and (b). Clearly, the harmonics in Fig. 7(c) can be divided into two groups as derived: 1) around ω_h, $3\omega_h$, $5\omega_h$, etc., which are around 50, 150, 250 Hz, etc.; the dominant harmonics in this group are around 50 Hz; 2) around $2\omega_h$, $4\omega_h$, $6\omega_h$, etc., which are around 100, 200, 300 Hz, etc.; the dominant harmonics in this group are around 100 Hz. To give a clear look of the dominant harmonics in Fig. 7(c), the expanded FFT results of the harmonics around 50 and 100 Hz are given in Fig. 8. Fig. 8(a) shows the harmonics around 50 Hz, and the dominate components are 46 and 54 Hz, which are the same as the theoretical calculated $\omega_h - 2\omega$ and $\omega_h + 2\omega$. The harmonics around 100 Hz are shown in Fig. 8(b), and the 98 and 102 Hz harmonics are the biggest components, which also prove the proposed expressions $2\omega_h + \omega$ and $2\omega_h - \omega$. As a result, the simulation results evidently verify the proposed analysis and derivations of the output harmonics in terms of the frequencies and the dominant components. Therefore, the proposed expressions of the harmonics can be an accurate and useful reference for the controller design. Meanwhile, after using the proposed suppression, it can be observed from the FFT analysis in Fig. 7(d) that the harmonic distortion of the output currents is significantly reduced, and the THD is decreased to only 2.81% from 8.78% in Fig. 7(c) without the proposed method, demonstrating the satisfying output control

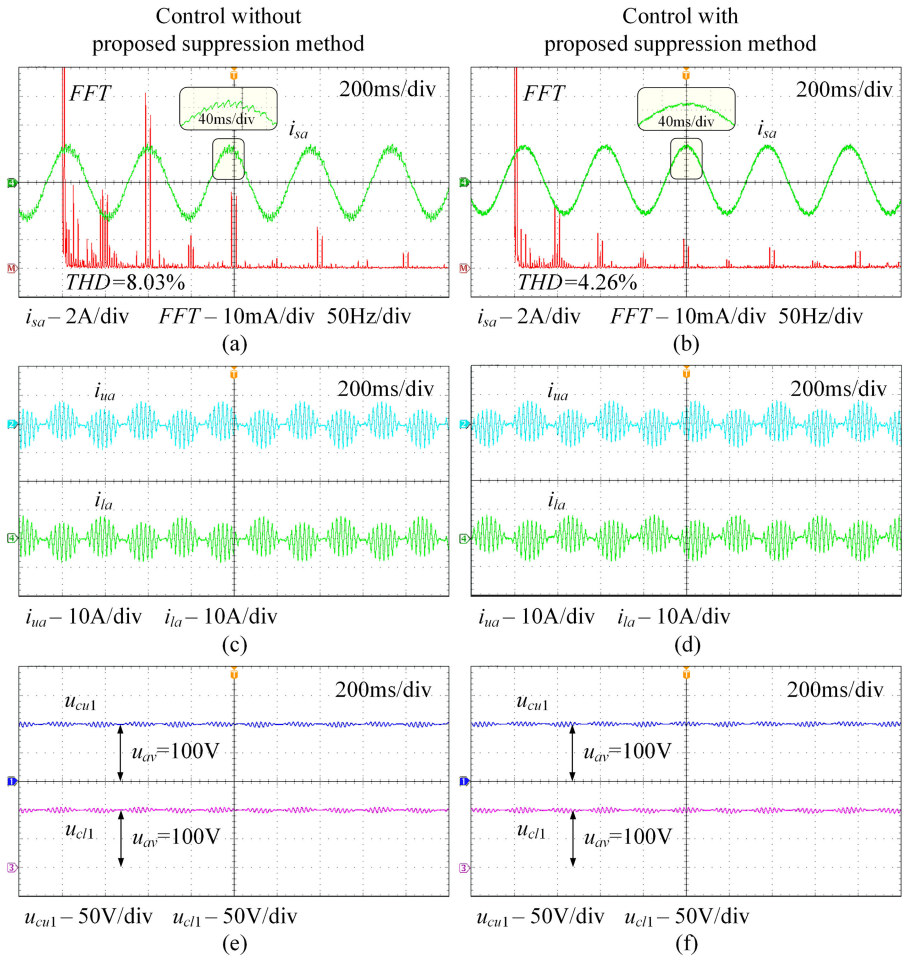

Fig. 11. Steady-state comparison results of the control without and with the proposed suppression method when $n = 57.2$ r/min and $\omega_h = 314$ rad/s.

performances for the motor. Besides, the arm currents in Fig. 7(e) and (f) and the capacitor voltages in upper and lower arms in Fig. 7(g) and (h) indicate little differences, because the suppressed harmonics are too small in comparison with the dominant injected components and fundamental components in the arms. Hence, the proposed suppression method only improves the output characteristics, and it has no unsatisfying influences on the inner quantities of MMC such as the arm currents and capacitor voltages.

The simulated waveforms of the motor speed ω_m and electromagnetic torque T_e are given in Fig. 7. The speeds in Fig. 7(i) and (j) are controlled at 3.4 rad/s, and the electromagnetic torques in Fig. 7(k) and (l) are controlled at 50% of the nominal torque. Obviously, with the reduced output distortion, the ripples of the motor speed in Fig. 7(j) and the electromagnetic torque in Fig. 7(l) with the proposed strategy are greatly reduced in comparison with the Fig. 7(i) and (k), demonstrating superior output performances of the proposed strategy. The dc current $i_{\rm dc}$ of the constant dc voltage source is given in Fig. 7(m) and (n). The ripple of $i_{\rm dc}$ in Fig. 7(n) of the proposed method is slightly larger than the traditional $i_{\rm dc}$ in Fig. 7(m). The dc voltage $U_{\rm dc}$ is a constant, and the capacitor voltage ripples have little changes. Therefore, the ripple of the input power in the proposed method only changes a little, while the ripple of the output power in terms of the speed and torque of the motor is evidently reduced by the proposed suppression. In that sense, the loss is reduced, and the efficiency consequently increases in virtue of the greatly improved output control performances. As a result, the proposed strategy focuses on the suppression of the output harmonic currents, and it effectively reduces the ripples of the speed and torque of the motor for desirable control performances, and thus reduces the loss caused by the ripples with improved efficiency.

In conclusion, the simulation results clearly prove the validity and the effectiveness of the proposed analysis of the harmonic components and the suppression method.

V. Experimental Results

The proposed analysis and suppression method are also verified by a downscaled prototype of a motor drive with MMC. Fig. 9 shows the photograph of the experimental setup, and the overview of the MMC prototype in the photo is given in Fig. 10. The MMC drives the induction motor, and the induction motor further drives the dc generators with the load resistors. Thus, the energy is finally consumed by the resistors and the torque

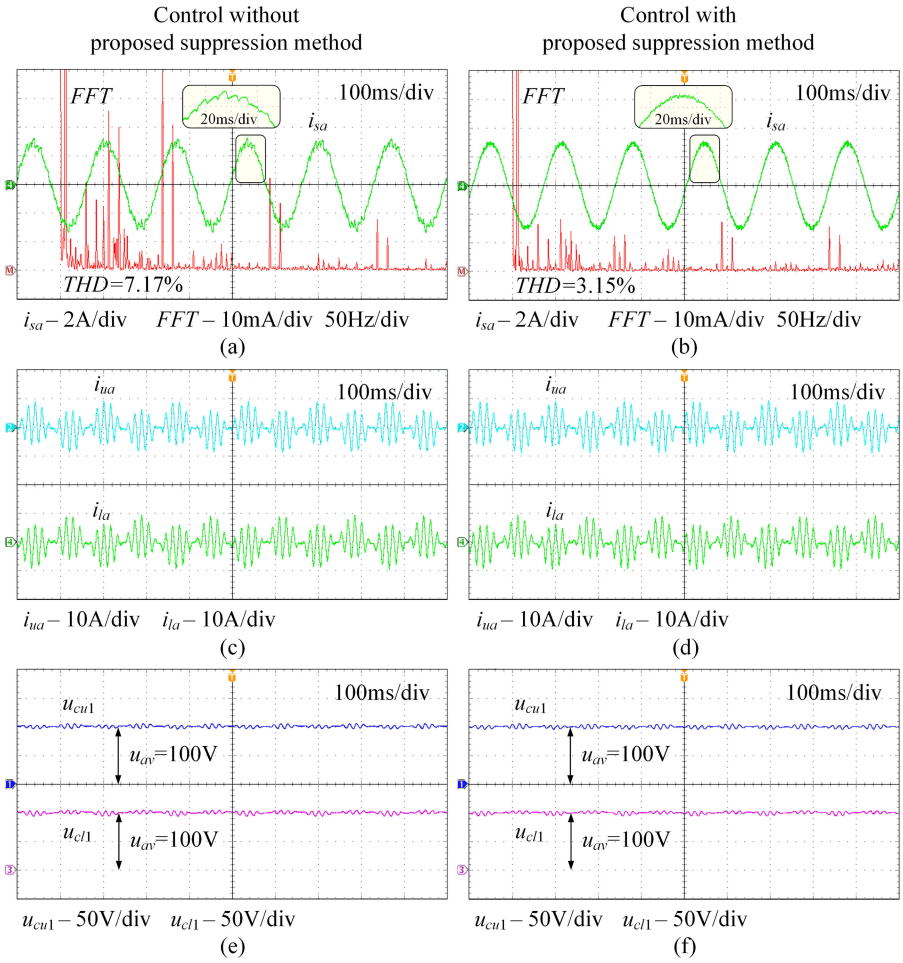

Fig. 12. Steady-state comparison results of the control without and with the proposed suppression method when $n = 143$ r/min and $\omega_h = 393$ rad/s.

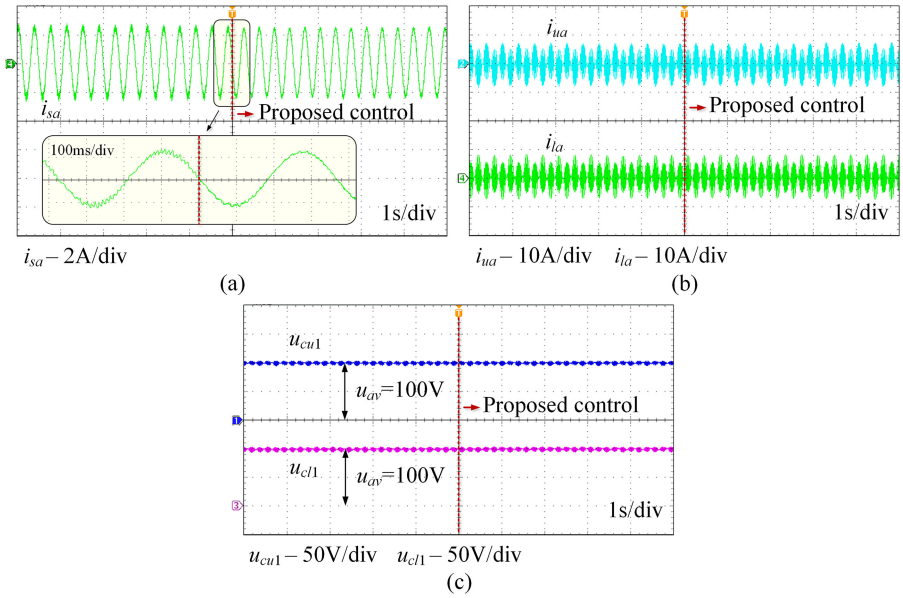

Fig. 13. Experimental results of switching on the proposed suppression method.

can be loaded on the induction motor. The specific parameters of the experimental setup are given in Table III. To reduce the low-frequency fluctuation, the conventional injection method [10] is applied, and the comparison results of the control without and with the proposed suppression method are presented to prove the validity. The transient and steady-state experimental waveforms are given in the following.

A. Steady-State Experimental Waveforms

The first group of the steady-state comparison results of the control without and with the proposed suppression method when $n = 57.2$ r/min and $\omega_h = 314\,\mathrm{rad/s}$ are given in Fig. 11. Since the speed of the motor is very low and the load resistors are limited, the load torque for the induction motor is set to be 50% rated value. Thus, the measured frequency of the output currents is very close to 2.7 Hz ($\omega = 2\pi \times 2.7 = 5.4\pi$). Meanwhile, the frequency of the injected components is 50 Hz. According to the proposed analysis, the dominant harmonics should be around ω_h and $2\omega_h$. However, the modulation *M* is small since the speed is very low and the load torque is half of the nominal, consequently the harmonics around $2\omega_h$ are clearly larger than the harmonics around ω_h.

Fig. 11(a) shows the output current of phase *a* and its FFT analysis calculated by the oscilloscope of the control without the proposed control. The output current is clearly distorted by the injection shown in the expanded waveforms of the peak current in Fig. 11(a). The FFT analysis of the output current in Fig. 11(a) shows that the harmonics can be divided into two groups as derived—1) around ω_h, $3\omega_h$, $5\omega_h$, etc., which are around 50, 150, 250 Hz, etc.; the dominant harmonics in this group are around 50 Hz; 2) around $2\omega_h$, $4\omega_h$, $6\omega_h$, etc., which are around 100, 200, 300 Hz, etc.; the dominant harmonics in this group are around 100 Hz. The frequencies of the largest harmonics in Fig. 11(a) are very close to 97.3 and 102.7 Hz ($2\omega_h + \omega$ and $2\omega_h - \omega$, $\omega = 2\pi \times 2.7 = 5.4\pi$, $\omega_h = 2\pi \times 50 = 100\pi$), and the harmonics around ω_h are smaller than the $2\omega_h$ harmonics since the modulation *M* is comparatively small. Apparently, the harmonic components in Fig. 11(a) are more complicated than the proposed analysis since the non-ideal factors of the devices and controllers are counted, such as the asymmetry of device parameters in three phases, and the resolution ratio of the FFT in oscilloscope is finite. However, most existing harmonics of the two groups in Fig. 11(a) including the dominant components are the same as the proposed analysis, demonstrating the correctness and validity of the derivations and providing a great reference for the suppression controller design.

After applying the proposed suppression method, the output current of phase *a* and the FFT analysis are given in Fig. 11(b). It can be observed that the distortion of the current is evidently reduced as shown in the expanded waveforms of the peak current in Fig. 11(b). The FFT results indicate that all the harmonics caused by the injections are suppressed, and the dominant harmonics of 97.3 and 102.7 Hz are cut by 80%. The THD of the output current using the proposed suppression is 4.26%, while the THD of the output current in Fig. 11(a) is as high as 8.03%. Certainly, the THD in Fig. 11(a) and (b) contains the harmonics of the switching frequencies, but as claimed before, this paper focuses on the harmonics caused by the injection, and the harmonics of the switching frequencies or caused by other non-ideal factors are not discussed and studied. As a result, the output harmonic current can be significantly suppressed by the proposed control with a clear drop on THD. Meanwhile, the arm currents are shown in Fig. 11(c) and (d), and the capacitor voltages on upper and lower arms are shown in Fig. 11(e) and (f), and they indicate little differences, since the suppressed harmonics are too small in comparison with the dominant injected components and fundamental components in the arms. Hence, the proposed control has no undesirable influence on the inner characteristics such as the arm currents and capacitor voltages.

The second group of the steady-state comparison results of the control without and with the proposed suppression method when $n = 143$ r/min and $\omega_h = 393\,\mathrm{rad/s}$ are given in Fig. 12. The actual measured frequency of the output current is nearly 5.9 Hz, and the frequency of the injected components is 62.5 Hz. The load torque is increased and set to be 70% rated value. The modulation *M* is larger in these conditions since both the speed and load torque are increased, thus the proportion of the harmonics around ω_h should also increase.

Fig. 12(a) shows the output current of the control without the proposed suppression and its FFT analysis. Similarly, the output current is also distorted by the injection in this situation. The FFT analysis results show the two groups of the harmonics: 1) around ω_h, $3\omega_h$, $5\omega_h$, etc., which are around 62.5, 187.5, 312.5 Hz, etc.; the dominant harmonics in this group are around 62.5 Hz; 2) around $2\omega_h$, $4\omega_h$, $6\omega_h$, etc., which are around 125, 250, 375 Hz, etc.; the dominant harmonics in this group are around 125 Hz. The frequencies of the largest harmonics are very close to 119.1 and 130.9 Hz ($2\omega_h$–ω and $2\omega_h + \omega$, $\omega = 2\pi \times 5.9 = 11.8\pi$, $\omega_h = 2\pi \times 62.5 = 125\pi$). Besides, the proportion of the harmonics around ω_h is clearly increased in comparisons with the first group waveforms in Fig. 11(a) since the modulation *M* is larger. As a result, with the acceptable errors, the FFT analysis results evidently prove the validity of the proposed derivations of the harmonic components in the output currents.

Fig. 12(b) shows the output current and the FFT analysis of applying the proposed suppression control. It can be seen from the FFT results that all the harmonic currents are effectively reduced, and the THD is 3.15%, cut by more than half in comparison with the 7.17% in Fig. 12(a). Consequently, the performances of the output currents are improved when the proposed suppression method is used. Similarly, according to the comparison results of the arm currents in Fig. 12(c) and (d) and the capacitor voltages in Fig. 12(e) and (f), the proposed control focuses on the output behaviors and has no adverse influence on the arm currents and capacitor voltages.

In conclusion, the steady-state experimental comparison results evidently verify the correctness and effectiveness of the proposed analysis for the output harmonics and the suppression method. The output harmonic currents are greatly reduced with more than half of the THD, demonstrating satisfying performances for the motor brought by the proposed control.

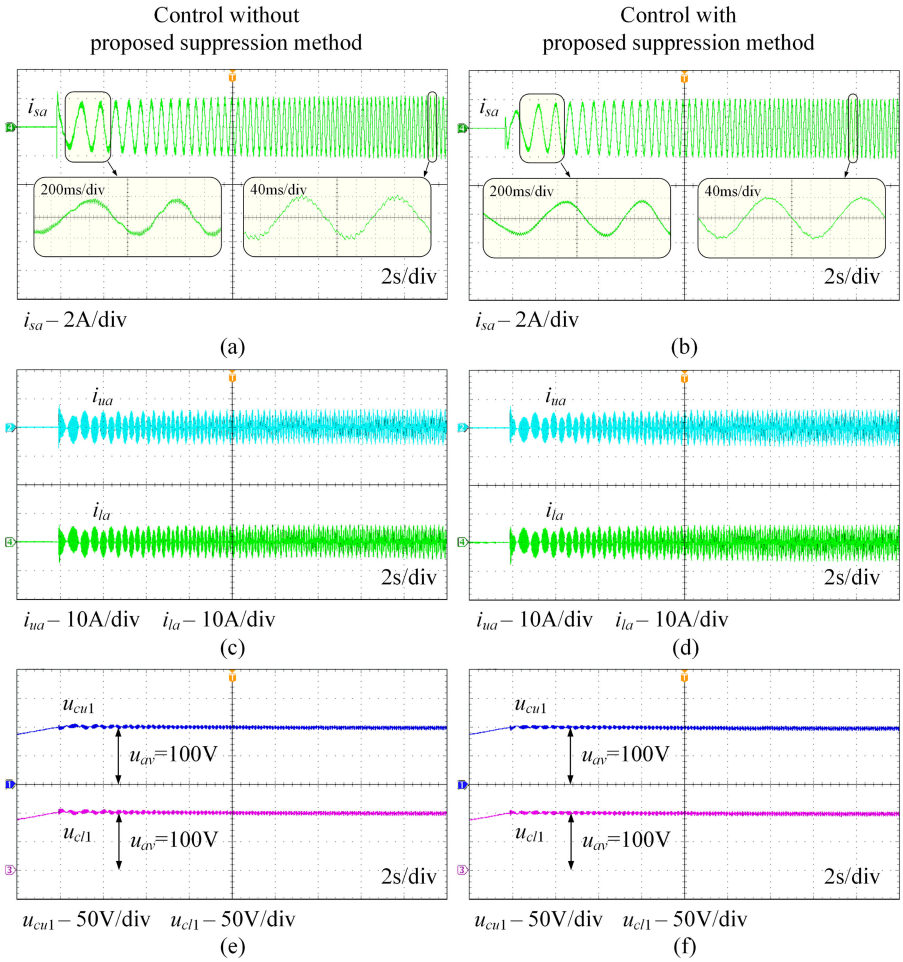

Fig. 14. Comparison results of the start-up process of control without and with the proposed suppression method.

B. Experimental Waveforms of the Transient Performances

The first group of the experimental results of switching on the proposed suppression method is given in Fig. 13. The conditions are the same as the first group of the steady-state waveforms: $n = 57.2$ r/min, $\omega_h = 314$ rad/s, and the load torque is half of the rated value. The system starts without the proposed control, and the proposed suppression control is switched on at the middle of the waveforms, and the detailed time instant for starting the proposed method is shown as the red dashed line in Fig. 13. The output current is shown in Fig. 13(a), and the current is obviously distorted by the injection. After the proposed control is switched ON, the harmonics are suppressed rapidly as shown in the expanded waveforms near the switched point, and the operation process is fast and smooth without any overshoot or oscillations. What is more, the amplitude of the output current is also reduced after using the proposed method due to the decrease of the harmonics. Meanwhile, the arm currents in Fig. 13(b) and the capacitor voltages in Fig. 13(c) demonstrate no overshoot or oscillation either when switching ON the proposed control, since it only changes the output characteristics. Consequently, the dynamic waveforms in Fig. 13 prove the fast responses of the proposed suppression control and reliable performances for improving the output currents.

Fig. 14 shows the experimental comparison results of the start-up process of control without and with the proposed suppression method. For both groups, the motor starts from standstill to 143 r/min, and the frequency of the injected components is 50 Hz.

Fig. 14(a) shows the output current of the control without the proposed method. It can be observed from the two expanded waveforms in Fig. 14(a) that the current is clearly distorted. Meanwhile, using the proposed suppression method, the output harmonic currents in Fig. 14(b) are effectively reduced as shown in the expanded figures. Generally, with the increase of the speed, a delay caused by the LPF in the proposed control will appear and lead to the inaccuracy of the harmonic detection. Nevertheless, the inertia of the motor is normally quite large, and the response of the speed is not very fast in comparison with the control periods, thus the delay in the harmonic detection can be totally accepted as shown in Fig. 14(b). Therefore, the proposed suppression method can be applied in the start-up process or other situations that the speed changes with satisfying effects on the output currents. Besides, the arm currents in Fig. 14(c) and (d) and the capacitor voltages in Fig. 14(e) and (f) show little differences, since the suppressed harmonics are too small in comparison with the dominant injected components and fundamental components in the arms, which indicates that

the proposed method only focuses on improving the output characteristics. Consequently, the comparison results of the start-up process in Fig. 14 prove that the proposed control is qualified in the start-up process to evidently suppress the harmonics in the output currents.

VI. Conclusion

This paper studied and derived the novel comprehensive relations between the output harmonic currents and the inner characteristics caused by the injection method for the low-frequency fluctuation, and the essential reason for the distorted output currents is revealed with the theoretical proof. The existing output harmonics are summarized, and the expressions of the dominant components are also derived, which gives an accurate reference for the controller design. What is more, this paper proposes a new suppression method that effectively reduces the output harmonic currents with greatly decreased THD for favorable output performances and improved efficiency. Combining the feedback and feedforward control, the proposed method is simple and practical with fast responses and reliable behaviors. The simulation results on PSCAD/EMTDC and experimental results on an experimental setup of MMC-based motor drive prove the validity and correctness of the presented analysis and calculations of the output harmonics, and the harmonics in the output currents are definitely suppressed by the proposed method for half reduced THD with satisfying dynamic responses and reliable performances.

In conclusion, the presented analysis gives an in-depth study of the output current distortion and provides an accurate and useful reference for the controller design. The proposed suppression control is greatly suitable and efficient for the applications of MV variable-speed drive with MMC, especially for the superior output harmonic characteristics in the low-frequency region. To achieve greater control performances, more research on advanced controllers and parameter designing based on an accurate and practical system model can be studied in future.

References

[1] D. Zhou, S. Yang, and Y. Tang, "A voltage-based open-circuit fault detection and isolation approach for modular multilevel converters with model-predictive control," *IEEE Trans. Power Electron.*, vol. 33, no. 11, pp. 9866–9874, Nov. 2018.

[2] X. Liu *et al.*, "A novel diode-clamped modular multilevel converter with simplified capacitor voltage-balancing control," *IEEE Trans. Ind. Electron.*, vol. 64, no. 11, pp. 8843–8854, Nov. 2017.

[3] J. Huang *et al.*, "Priority sorting approach for modular multilevel converter based on simplified model predictive control," *IEEE Trans. Ind. Electron.*, vol. 65, no. 6, pp. 4819–4830, Jun. 2018.

[4] F. Zhao, G. Xiao, and T. Zhao, "Accurate steady-state mathematical models of arm and line harmonic characteristics for modular multilevel converter," *IEEE Trans. Power Del.*, vol. 33, no. 3, pp. 1308–1318, Jun. 2018.

[5] J. Wang and P. Wang, "Power decoupling control for modular multilevel converter," *IEEE Trans. Power Electron.*, vol. 33, no. 11, pp. 9296–9309, Nov. 2018.

[6] B. Gutierrez and S. Kwak, "Modular multilevel converters (MMCs) controlled by model predictive control with reduced calculation burden," *IEEE Trans. Power Electron.*, vol. 33, no. 11, pp. 9176–9187, Nov. 2018.

[7] A. Marzoughi, R. Burgos, D. Boroyevich, and Y. Xue, "Design and comparison of cascaded H-bridge, modular multilevel converter, and 5-L active neutral point clamped topologies for motor drive applications," *IEEE Trans. Ind. Appl.*, vol. 54, no. 2, pp. 1404–1413, Mar./Apr. 2018.

[8] A. Antonopoulos, L. Ängquist, S. Norrga, K. Ilves, L. Harnefors, and H.-P. Nee, "Modular multilevel converter AC motor drives with constant torque from zero to nominal speed," *IEEE Trans. Ind. Appl.*, vol. 50, no. 3, pp. 1982–1993, May/Jun. 2014.

[9] K. Wang, Y. Li, Z. Zheng, and L. Xu, "Voltage balancing and fluctuation-suppression methods of floating capacitors in a new modular multilevel converter," *IEEE Trans. Ind. Electron.*, vol. 60, no. 5, pp. 1943–1954, May 2013.

[10] M. Hagiwara, I. Hasegawa, and H. Akagi, "Start-up and low-speed operation of an electric motor driven by a modular multilevel cascade inverter," *IEEE Trans. Ind. Appl.*, vol. 49, no. 4, pp. 1556–1565, Jul./Aug. 2013.

[11] B. Li *et al.*, "An improved circulating current injection method for modular multilevel converters in variable-speed drives," *IEEE Trans. Ind. Electron.*, vol. 63, no. 11, pp. 7215–7225, Nov. 2016.

[12] J. Jung, H. Lee, and S. Sul, "Control strategy for improved dynamic performance of variable-speed drives with modular multilevel converter," *IEEE J. Emerg. Sel. Topics Power Electron.*, vol. 3, no. 2, pp. 371–380, Jun. 2015.

[13] L. He, K. Zhang, J. Xiong, S. Fan, and Y. Xue, "Low-frequency ripple suppression for medium-voltage dives using modular multilevel converter with full-bridge submodules," *IEEE J. Emerg. Sel. Topics Power Electron.*, vol. 4, no. 2, pp. 657–667, Jun. 2016.

[14] S. Debnath and M. Saeedifard, "Optimal control of modular multilevel converters for low-speed operation of motor drives," in *Proc. IEEE Appl. Power Electron. Conf. Expo.*, Mar. 2014, pp. 247–254.

[15] S. Debnath, J. Qin, and M. Saeedifard, "Control and stability analysis of modular multilevel converter under low-frequency operation," *IEEE Trans. Ind. Electron.*, vol. 62, no. 9, pp. 5329–5339, Sep. 2015.

[16] S. Du, B. Wu, N. Zargari, and Z. Cheng, "A flying-capacitor modular multilevel converter for medium-voltage motor drive," *IEEE Trans. Power Electron.*, vol. 32, no. 3, pp. 2081–2089, Mar. 2016.

[17] S. Du, B. Wu, and N. R. Zargari, "A startup method for flying-capacitor modular multilevel converter (FC-MMC) with effective damping of LC oscillations," *IEEE Trans. Power Electron.*, vol. 32, no. 7, pp. 5827–5834, Jul. 2017.

[18] M. Hagiwara and H. Akagi, "Control and experiment of pulsewidth-modulated modular multilevel converters," *IEEE Trans. Power Electron.*, vol. 24, no. 7, pp. 1737–1746, Jul. 2009.

[19] B. K. Bose, Ed., *Power Electronics and Variable Frequency Drives*. New York, NY, USA: IEEE Press, 1996.

[20] A. Munoz-Garcia, T. A. Lipo, and D. W. Novotny, "A new induction motor V/f control method capable of high-performance regulation at low speeds," *IEEE Trans. Ind. Appl.*, vol. 34, no. 4, pp. 813–821, Jul./Aug. 1998.

[21] F. Blaschke, "The principle of field-orientation as applied to the transvector closed-loop control system for rotating-field machines," *Siemens Rev.*, vol. 34, pp. 217–220, 1972.

[22] K. Hasse, "Drehzahlgelverfahren für schnelle umkehrantriebe mit stromrichtergespeisten asynchron-kurzschlusslaufer-motoren," *Reglungstechnik*, vol. 20, pp. 60–66, 1972.

[23] I. Takahashi and T. Noguchi, "A new quick-response and high-efficiency control strategy of an induction motor," *IEEE Trans. Ind. Appl.*, vol. IA-22, no. 5, pp. 820–827, Sep. 1986.

[24] M. Depenbrock, "Direct self-control (DSC) of inverter-fed induction machine," *IEEE Trans. Power Electron.*, vol. 3, no. 4, pp. 420–429, Oct. 1988.

[25] H. Mao, D. Boroyevich, and F. C. Lee, "Novel reduced-order smallsignal model of a three-phase PWM rectifier and its application in control design and system analysis," *IEEE Trans. Power Electron.*, vol. 13, no. 3, pp. 511–521, May 1998.

[26] H. Akagi, "New trends in active filters for power conditioning," *IEEE Trans. Ind. Appl.*, vol. 32, no. 6, pp. 1312–1322, Nov./Dec. 1996.

[27] H. Akagi, Y. Kanazawa, and A. Nabae, "Instantaneous reactive power compensators comprising switching devices without energy storage components," *IEEE Trans. Ind. Appl.*, vol. IA-20, no. 3, pp. 625–630, May 1984.

[28] H. Akagi, A. Nabae, and S. Atoh, "Control strategy of active power filters using multiple voltage-source PWM converters," *IEEE Trans. Ind. Appl.*, vol. IA-22, no. 3, pp. 460–465, May 1986.

[29] S. Bhattacharya and D. Divan, "Synchronous frame based controller implementation for a hybrid series active filter system," in *Proc. IEEE/IAS Annu. Meeting*, Orlando, FL, USA, pp. 2531–2540.

Fangzhou Zhao was born in Jinan, China, in 1992. He received the B.S. degree in electrical engineering and automation from the University of Electronic Science and Technology of China, Chengdu, China, in 2014. He is currently working toward the Ph.D. degree at the Power Electronics and Renewable Energy Center, School of Electrical Engineering, Xi'an Jiaotong University (XJTU), Xi'an, China.

His research interests include model, design, and control of modular multilevel converters and applications of wide band-gap devices. He is with the State Key Laboratory of Electrical Insulation and Power Equipment, School of Electrical Engineering, XJTU.

Guochun Xiao (M'06) was born in Sichuan, China, in 1965. He received the B.S., M.S., and Ph.D. degrees from the School of Electrical Engineering, Xi'an Jiaotong University, Xi'an, China, in 1987, 1990, and 2002, respectively.

From 1990 to 1998, he was an Engineer with the Xi'an Electric Furnace Research Institute. He is currently a Full Professor with Xi'an Jiaotong University. His current research interests include power conversion systems, harmonics suppression, reactive power compensation, active power filters, and control of modular multilevel converters.

Tianhua Zhu (S'16) was born in Anhui, China, in 1992. She received the B.S. and M.S. degrees in electrical engineering from Xi'an Jiaotong University (XJTU), Xi'an, China, in 2014 and 2017, respectively. She is currently working toward the Doctor's degree at the Power Electronics and Renewable Energy Center (PEREC), XJTU.

Her current research interests include characteristics and application of wide band-gap devices, maximum power point tracking techniques, and distributed maximum power point tracking. She is with the State Key Laboratory of Electrical Insulation and Power Equipment, School of Electrical Engineering, XJTU.

Tong Zhao was born in Taian, China. He received the Ph.D. degree in control science and engineering professional from Shanghai Jiaotong University, Shanghai, China, in 2005.

He is currently a Full Professor with the College of Automation and Electronic Engineering, Qingdao University of Science and Technology, Qingdao, China. His research interests include intelligent control and model, and control of nonlinear systems.

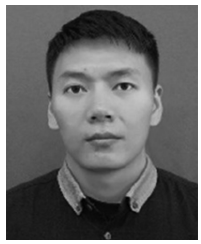

Xu Zheng was born in Shuozhou, China. He received the B.S. degree in electrical engineering from Xi'an Jiaotong University (XJTU), Xi'an, China, in 2017. He is currently working toward the M.S degree at the School of Electrical Engineering, XJTU.

His research interests include control of modular multilevel converters.

Zhiqian Wu was born in Yiwu, China. He received the B.S. degree in electrical engineering from Xi'an Jiaotong University (XJTU), Xi'an, China, in 2018. He is currently working toward the M.S. degree in the School of Electrical Engineering, XJTU.

His research interests include control of modular multilevel converters.